

Cite this: *Nanoscale*, 2016, 8, 2434

Synthesis of aligned symmetrical multifaceted monolayer hexagonal boron nitride single crystals on resolidified copper†

Roland Yingjie Tay,^{a,b} Hyo Ju Park,^c Gyeong Hee Ryu,^c Dunlin Tan,^{a,d}
Siu Hon Tsang,^b Hongling Li,^{a,d} Wenwen Liu,^a Edwin Hang Tong Teo,^{*a,e}
Zonghoon Lee,^{c,f} Yeshayahu Lifshitz^g and Rodney S. Ruoff^{f,h}

Atomically smooth hexagonal boron nitride (h-BN) films are considered as a nearly ideal dielectric interface for two-dimensional (2D) heterostructure devices. Reported mono- to few-layer 2D h-BN films, however, are mostly small grain-sized, polycrystalline and randomly oriented. Here we report the growth of centimetre-sized atomically thin h-BN films composed of aligned domains on resolidified Cu. The films consist of monolayer single crystalline triangular and hexagonal domains with size of up to ~10 μm . The domains converge to symmetrical multifaceted shapes such as "butterfly" and "6-apex-star" and exhibit ~75% grain alignment for over millimetre distances as verified through transmission electron microscopy. Scanning electron microscopy images reveal that these domains are aligned for over centimetre distances. Defect lines are generated along the grain boundaries of mirroring h-BN domains due to the two different polarities (BN and NB) and edges with the same termination. The observed triangular domains with truncated edges and alternatively hexagonal domains are in accordance with Wulff shapes that have minimum edge energy. This work provides an extensive study on the aligned growth of h-BN single crystals over large distances and highlights the obstacles that are needed to be overcome for a 2D material with a binary configuration.

Received 14th November 2015,
Accepted 30th December 2015

DOI: 10.1039/c5nr08036c

www.rsc.org/nanoscale

Introduction

Hexagonal boron nitride (h-BN) is a synthetic crystalline material with alternating boron (B) and nitrogen (N) atoms bonded in a honeycomb lattice structure that is stacked in an AA' configuration. Being electrically insulating as well as

chemically and thermally stable, atomically thin h-BN films including monolayers have been used as dielectric or substrate layers for other two-dimensional (2D) materials such as graphene and transition metal dichalcogenides (TMDs) which exhibit excellent performance due to their ultra-smooth surface and low density of dangling bonds.¹ h-BN films are also used as an ultra-thin spacer layer for metal-insulator-metal (MIM) structures and a tunnelling barrier for electrons enabling a wide range of applications such as nanocapacitors and field-effect tunnelling transistors.^{2,3} Motivated by the need for up-scaling, centimetre-scale syntheses of polycrystalline ultra-thin continuous h-BN films by chemical vapour deposition (CVD) on various transition metals have been explored.^{4–9} The prolific nucleation and growth of mis-oriented domains on polycrystalline metal surfaces, however, leads to the formation of grain boundary defects by coalescence.¹⁰

Two strategies are important to realise high quality large-area growth of h-BN films, akin to graphene growth.^{11,12} The first is to suppress the amount of nucleation and thus obtain larger domains.^{13–17} This can be achieved through process optimization by controlling the CVD parameters,^{16–21} and enhancing other external factors such as smoothening the substrate surface and enlargement of Cu grains.^{13,22} More significantly, it has been observed recently that the inclusion of Ni

^aSchool of Electrical and Electronic Engineering, Nanyang Technological University, 50 Nanyang Avenue, Singapore 639798, Singapore. E-mail: httee@ntu.edu.sg

^bTemasek Laboratories@NTU, 50 Nanyang Avenue, Singapore 639798, Singapore

^cSchool of Materials Science and Engineering, Ulsan National Institute of Science and Technology (UNIST), Ulsan 689-798, Republic of Korea

^dCNRS-International NTU Thales Research Alliance CINTRA UMI 3288, Research Techno Plaza, 50 Nanyang Drive, Singapore 637553, Singapore

^eSchool of Materials Science and Engineering, Nanyang Technological University, 50 Nanyang Avenue, Singapore 639798, Singapore

^fCenter for Multidimensional Carbon Materials, Institute for Basic Science (IBS), Ulsan 689-798, Republic of Korea

^gDepartment of Materials Science and Engineering, Technion, Israel Institute of Technology, Haifa 3200003, Israel

^hDepartment of Chemistry, Ulsan National Institute of Science and Technology (UNIST), Ulsan 689-798, Republic of Korea

†Electronic supplementary information (ESI) available: Additional SEM and AFM images of h-BN films grown using various conditions. Optical and AFM images of different Cu surfaces, characterisation of annealed W foil and TEM/SAED survey of the h-BN films. See DOI: 10.1039/c5nr08036c

into a Cu substrate can further increase the size of the domains by suppressing both the nucleation and growth rate due to a different growth mechanism based on solid-gas reactions involving surface chemistry of Ni-B and Ni-N.¹⁴ However, this strategy becomes more difficult with bigger crystal sizes beyond the millimetre regimes. The second is to consider the stitching of these individual domains into a mosaic-type film where most of the domains are aligned.¹² A mosaic crystal is essentially polycrystalline which is formed by the coalescence of grains with the same orientation. Although seamless stitching between oriented graphene domains has been well-reported owing to its unary configuration,¹¹ the in-plane coalescence between h-BN domains is much more complicated due to its binary nature. While most of the previous studies to date focused on the former strategy, here we report the growth of aligned h-BN domains for over centimetre distances on resolidified Cu.

Islands of single-crystal h-BN domains with dimensions exceeding 100 μm grown by CVD on Ni,^{23–25} Cu,^{4,13,18,22} Pt,²⁶ Au,²⁷ Fe¹⁵ and Cu-Ni alloy¹⁴ have been reported and aligned growth of h-BN domains has been observed on both Ni and Cu with (111) surface orientation.^{23,24,28} It has been demonstrated that h-BN domains exhibit a strict epitaxial relationship with the Cu lattice with highly ordered arrangements^{28–30} due to the relatively weak interaction between h-BN and Cu.³¹ Hence, one good approach to obtain a highly uniform Cu surface is by melting the growth substrate.^{32–39} In this work, we prepared single-crystal Cu with (110) surface orientation by melting and resolidifying polycrystalline Cu foils on a W foil. Unlike the growth on typical polycrystalline Cu foils where the h-BN domains nucleate with more orientations,^{4,22} the h-BN domains here nucleate and grow with a dominant crystal orientation over the entire resolidified Cu surface. Selected area electron diffraction (SAED) together with dark-field (DF) transmission electron microscopy (TEM) investigations revealed that the orientations of the h-BN domains are predominantly consistent with $\sim 75\%$ grain alignment of up to millimetre-range. Furthermore, using scanning electron microscopy (SEM) to map the larger surface area, the h-BN domains were also found to be consistently aligned over centimetre distances as well. A variety of symmetrical multifaceted shapes of the h-BN domains are achieved by the convergence of oriented domains with defect lines forming at the boundaries between merged mirroring domains. The observed triangular domains with truncated edges and alternatively hexagonal domains are rationalized with Wulff shapes that have minimum edge energy.

Experimental section

APCVD growth of h-BN on resolidified Cu

A 2 cm \times 1.5 cm W foil (Alfa Aesar, product no. 10417, 50 μm thick) was used as a supporting substrate for Cu. Three pieces of similar sized, 2 cm \times 1.5 cm, Cu foils (Alfa Aesar, product no. 13382, 25 μm thick) were first dipped into dilute nitric

acid for a few seconds followed by rinsing in DI water and blow-dried in nitrogen. Subsequently, these Cu foils were placed on top of the W foil and the entire stack was loaded into a 1 inch quartz tube. The temperature of the furnace was initially ramped up to 1000 $^{\circ}\text{C}$ in 50 min followed by an elevation to 1090 $^{\circ}\text{C}$ in another 10 min. This entire process was carried out under a constant Ar/H₂ flow of 200 : 5 sccm. At 1090 $^{\circ}\text{C}$, the Cu melted and wet the underlying W foil. The temperature was kept constant at 1090 $^{\circ}\text{C}$ for a further 30 min to ensure complete melting of the Cu foils and that they are uniformly spread on the W substrate. To resolidify the Cu prior to exposure to ammonia borane, the temperature was slowly decreased to 1075 $^{\circ}\text{C}$ at a rate of 1 $^{\circ}\text{C min}^{-1}$ and the temperature was stabilized for another 10 min. 8 mg of ammonia borane, which was placed in a ceramic boat upstream from the heating zone, was heated at 85 $^{\circ}\text{C}$ for a specified time. After growth, the temperature was quickly cooled by opening the lid of the furnace.

Characterisation

Scanning electron microscopy images (SEM, LEO 1550 Gemini) were obtained of the as-grown h-BN on Cu substrates. The percentage of few-layer islands on fully covered h-BN films were extracted using ImageJ software by differentiating the contrast in the SEM image between the monolayer base (darker contrast) and few-layer islands (lighter contrast). Energy dispersive spectroscopy (EDS, Oxford Instruments) was performed on an SEM (JEOL JSM-5600LV) using INCA software to determine the elemental composition of the resolidified Cu. Electron backscatter diffraction (EBSD, Oxford Instruments) was performed on an SEM (JEOL JSM-7600F) using Aztec software to determine the surface orientation of the resolidified Cu and W foils. Atomic force microscopy (AFM, Cypher scanning probe microscope) was performed using tapping mode to measure the thickness of the transferred h-BN films on SiO₂/Si substrates as well as the various Cu and W substrates. Transmission electron microscopy (TEM) imaging, selected area electron diffraction (SAED) and dark-field (DF) TEM mapping were performed on an aberration-corrected TEM (FEI Titan3TM G2 60–300) with an acceleration voltage of 80 kV to determine the h-BN crystal orientation of specific regions of the h-BN films and domains. High resolution (HR) TEM images were obtained with an exposure time of 0.2 s. SAED patterns were obtained at various positions for h-BN spanning holes having a 1.2 μm diameter. DF-TEM images were taken from one spot among six diffracted spots comprising the vertices of a regular hexagon using an objective aperture with a 1.28 nm^{−1} diameter for 7 s of acquisition time. Raman spectroscopy with laser excitation wavelength of 532 nm (Witec) at room temperature was used to determine the crystallinity of the h-BN film. X-ray photoelectron spectroscopy (XPS, VG ESCA 220i-XL Imaging) was used to determine the bonding and elemental compositions of the h-BN film. Ultraviolet-visible spectroscopy (UV-vis, Shimadzu UV-2450) was used to measure the OBG of the h-BN film.

Results and discussion

The growth methodology using atmospheric pressure (AP) CVD is illustrated in Fig. 1a and the details are described in the Experimental section. Cu foils were first melted on a W foil and the liquid Cu was resolidified before h-BN growth was performed by exposure to ammonia borane ($\text{NH}_3\text{-BH}_3$). Fig. 1b–d shows the SEM images of the as-grown h-BN domains with regular shapes such as triangles, asymmetric hexagons and hexagons on the resolidified Cu. It is observed that both the sublimation temperature and amount of ammonia borane used affect the nucleation density and the size of h-BN

domains,¹⁸ and both of which increase with higher sublimation temperature and amount of ammonia borane (Fig. S1 and S2†). Hence, in this study, we adopted an optimized set of parameters using 8 mg of ammonia borane which is heated at 85 °C under a constant Ar/ H_2 flow of 200 : 5 sccm during h-BN growth. The growth from isolated single-crystal domains to a continuous film can be controlled by increasing the growth time (Fig. S3†). Isolated single-crystal domains are grown during the initial 5 to 20 min. It is observed that both the amount of nucleation and the lateral size of the domains increase with growth time and the largest obtained single-crystal h-BN domain is $\sim 10\text{ }\mu\text{m}$ after 20 min of growth. Several

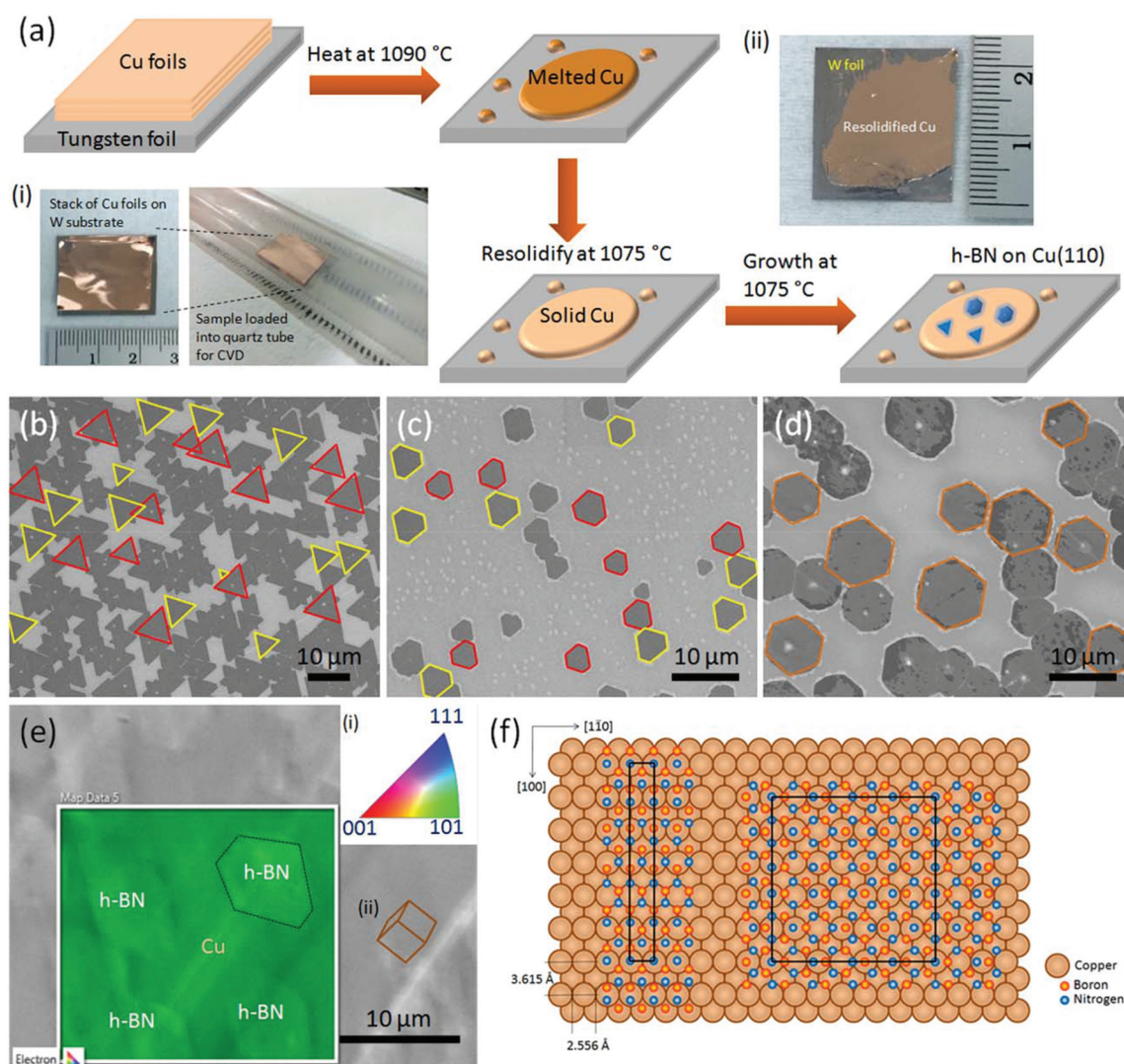


Fig. 1 Growth of aligned monolayer h-BN single crystals on resolidified Cu. (a) Schematic illustration of the *in situ* Cu treatment and CVD growth process for single-crystal h-BN domains. (ai) Photographs showing the preparation of the Cu/W stack loaded into the quartz tube and (aii) photograph of resolidified Cu on the W substrate after h-BN growth process. SEM images of the as-grown oriented (b) triangular, (c) asymmetric hexagonal and (d) hexagonal shaped h-BN domains, respectively. The red and yellow lines outline the h-BN domains which indicate 60° rotational difference from each other. Alignment of hexagonal shaped h-BN domains are outlined in orange. (e) Representative SEM/EBSD image of the as-grown hexagonal shaped h-BN domains on resolidified Cu at 70° tilt. (ei) Colour codex of the Cu lattice direction and (eii) a cubic representation of the unit Cu lattice cell with respect to the SEM image. (f) Schematic of the atomic arrangement of h-BN on Cu(110) with two different possible orientations. A (1 × 6) unit cell consisting of 10 BN pairs and a (7 × 5) unit cell consisting of 56 BN pairs are outlined in black.

bi- to few-layer islands can be observed in the h-BN films indicating that the growth is not self-limited in agreement with previous reports (Fig. S4†).^{4,18} These additional layers are proposed to be grown at the h-BN/Cu interface.²⁰ In order to reduce the amount of adlayers, a strict control of CVD parameters is required. As a higher amount of precursor tends to increase the nucleation rate, a controlled amount of precursor is used to achieve a full coverage film with fewer adlayers. For our CVD system, a full coverage film with ~2% adlayers can be achieved under optimal growth conditions (Fig. S3d†).

Another factor which affects the nucleation rate and the domain size is the roughness of the Cu substrates.²² As compared to commercially available Cu foils, the resolidified Cu has a very smooth surface morphology with no rolling features comprising of parallel uneven grooves (Fig. S5†). This leads to a slight enhancement in the domain sizes with a suppressed nucleation rate (Fig. S6†). It is evident that the as-grown h-BN single-crystal domains are well oriented for over centimetre ranges on the resolidified Cu as revealed by the SEM images which are composed of regular shapes such as triangles, asymmetric hexagons and hexagons (Fig. S7†). It is observed that these different domain shapes are distributed unevenly throughout the growth surface. The domains with the same shape (either triangle or hexagon) tend to coagulate into clusters exceeding 1 mm² in area, demonstrating that the shape of the domains could be due to substrate position effects.⁴⁰ The triangles and asymmetric hexagons have two orientations that are rotated by 60° from each other, as outlined in red and yellow in Fig. 1b and c. The 60° rotation is equivalent to 180° mirror symmetry resulting from the different polarities of B–N bonds (*i.e.* BN or NB) within the domains (Fig. S8†). SEM images show that both orientations are almost equally distributed, indicating that there is little or no preference to one particular h-BN orientation on the Cu surface.

To elucidate the crystallographic orientation of the Cu substrate, electron backscatter diffraction (EBSD) was used to map the surface orientation of the resolidified Cu after h-BN growth. Fig. 1e shows the representative SEM/EBSD mapping of the resolidified Cu surface tilted at 70°. It is clear that the entire surface of the resolidified Cu is (110) oriented (green mapping represents (101) orientation which is equivalent to (110) in Fig. 1e). Large-area scans showed the single crystalline nature of the Cu surface which extends over many millimetres (Fig. S9†). In our study, the Cu resolidifies into a (110) surface orientation similar to the report by Wu *et al.*³³ We note that other orientations may also be possible as reported by Mohsin *et al.* where Cu resolidifies into a (111) surface orientation.³⁴ Unlike the growth of Cu on the W(100) substrate where the Cu grows pseudomorphic up to two monolayers,^{41–43} the polycrystalline W foil used here does not affect the single-crystalline surface orientation of the resolidified Cu. It is observed that the W foil has small grain sizes of up to a few micrometres consisting of (100) and (111) surface orientations (Fig. S10†). After the Cu melting and resolidification processes, the polycrystalline property of the W foil remained almost

unchanged and its smooth surface led to the smooth morphology of the resolidified Cu.

Interestingly, distorted h-BN domains can be observed on the SEM/EBSD mapped image in Fig. 1e. One of these distorted h-BN domains is outlined for better visualisation. It should be noted that the distortion is due to the tilt angle (EBSD is commonly done at 70° tilt) during image capturing and is not indicative of the actual physical dimension of the h-BN domains. To visualise the Cu atomic configuration, a cubic representation of a Cu lattice unit cell is drawn corresponding to the SEM image (Fig. 1eii). Based on post-growth analysis, a static model as shown in Fig. 1f is proposed for the h-BN atomic configuration on Cu(110) surface with two different orientations (rotated by 30° with respect to each other). Their unit cells consisting of (1 × 6) and (7 × 5) structures are outlined in black, following Greber *et al.*, who grew a monolayer of h-BN on Ni(110) and the (1 × 6) supercells are more abundant with a relative weight of 6 : 1.⁴⁴

The lattice mis-match, M , is calculated using $M = (\alpha_f - \alpha_s)/\alpha_s$, where α_f is the 2D film lattice constant and α_s is the substrate lattice constant. Since $\alpha_{\text{h-BN}} = 2.504 \text{ \AA}$ and $\alpha_{\text{Cu(111)}} = 2.556 \text{ \AA}$, the mis-match of h-BN on Cu(111) is ~2%. For the (1 × 6) h-BN structure on Cu(110), there is one substrate lattice constant along $\bar{1}\bar{1}0$ and six substrate lattice constants along $[100]$. The measured mis-match along $[\bar{1}\bar{1}0]$, $M_{1\times 6}^{\bar{1}\bar{1}0} = -2\%$ ($\alpha_f = \alpha_{\text{h-BN}}$ and $\alpha_s = \alpha_{\text{Cu(111)}}$) and along $[100]$, $M_{1\times 6}^{100} = -0.01\%$ ($\alpha_f = 5\sqrt{3}\alpha_{\text{h-BN}}$ and $\alpha_s = 6\sqrt{2}\alpha_{\text{Cu(111)}}$). For the (7 × 5) h-BN structure on Cu(110) with seven substrate lattice constants along $[\bar{1}\bar{1}0]$ and five substrate lattice constants along $[100]$, the mis-match along $[\bar{1}\bar{1}0]$, $M_{7\times 5}^{\bar{1}\bar{1}0} = -3\%$ ($\alpha_f = 4\sqrt{3}\alpha_{\text{h-BN}}$ and $\alpha_s = 7\alpha_{\text{Cu(111)}}$) and along $[100]$, $M_{7\times 5}^{100} = -3\%$ ($\alpha_f = 7\alpha_{\text{h-BN}}$ and $\alpha_s = 5\sqrt{2}\alpha_{\text{Cu(111)}}$). Therefore, the orientation with smaller mis-match in the (1 × 6) h-BN structure should, at least per this line of reasoning, be the dominant configuration on Cu(110).

The growth of h-BN on liquid Cu and the surface morphologies of the resolidified Cu with different resolidification cooling rates are further explored. When h-BN growth is carried out on liquid Cu at 1090 °C, mis-oriented h-BN domains are obtained which tend to form clusters as shown in Fig. 2a. Although the growth mechanism of h-BN during the liquid Cu phase is undetermined, this growth pattern is similar to that of graphene,^{32,33,38} where the domains are closely packed together with small gaps between the adjacent domains (Fig. S11†).³⁹ In order to obtain well-oriented h-BN domains, the liquid Cu is first resolidified by lowering the temperature from 1090 °C to 1075 °C before growth. It is observed from the SEM images in Fig. 2b–d that the orientations of the h-BN domains grown on the resolidified Cu at different resolidification cooling rates are all aligned, indicating that the resolidification process is crucial to realise oriented h-BN growth. The effects of the Cu surface morphologies at different resolidification rates are investigated by optical microscopy and atomic force microscopy (AFM). Fig. 2e shows the optical image of the resolidified Cu after being immediately cooled from the liquid state (1090 °C). Cu grains of up to several millimetres with many uneven lines can be

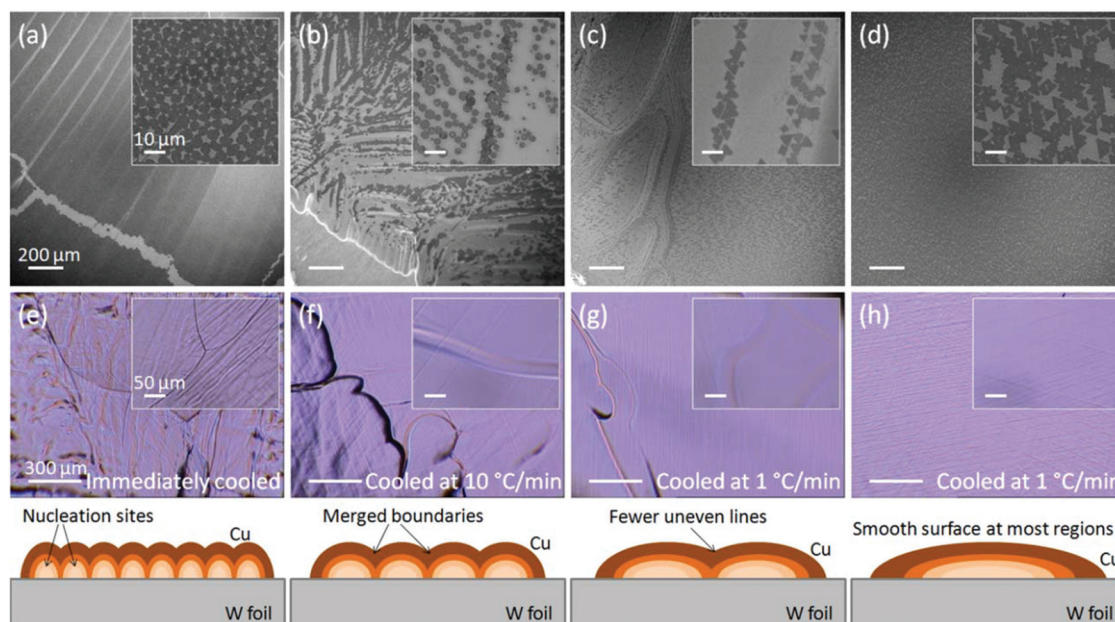


Fig. 2 Comparison of h-BN domains grown on liquid Cu and on resolidified Cu with different resolidification rates. SEM images of h-BN domains grown for 10 min on (a) liquid Cu at 1090 °C and on resolidified Cu at 1075 °C with a resolidification rate from 1090 °C to 1075 °C of (b) 10 °C min⁻¹ and (c, d) 1 °C min⁻¹. Scale bars are 200 μm. The insets of (a–d) show the corresponding magnified SEM images. Scale bars are 10 μm. (e–h) Optical images (top) and schematic illustrations (bottom) of the morphologies of the corresponding Cu substrates in (a–d), respectively. Scale bars are 300 μm. The insets of (e–h) show the corresponding magnified optical images. Scale bars are 50 μm.

observed. When the temperature drops below the melting point of Cu, recrystallization of the Cu begins on the W surface similar to the metal casting process.⁴⁵ This led to the formation of many nucleation sites of the Cu crystallites when the temperature is reduced very quickly. As the Cu resolidifies, the Cu crystals merged together forming grains and creating many uneven lines. AFM measurements show that the step difference in such uneven lines can reach up to ~1 μm (Fig. S12†). Visible differences on the Cu surface morphology can be observed, as shown in Fig. 2f–h, when Cu was allowed to resolidify before performing h-BN growth. By using a slower resolidification rate of 1 °C min⁻¹, significant reduction of these uneven lines is observed (Fig. S12†). However, these lines are difficult to be totally eliminated using our CVD system even when the cooling rate is further reduced to 0.1 °C min⁻¹. Most of these uneven lines resulted in no change in the orientation of the h-BN domains (Fig. S13†). The increased Cu surface roughness, however, led to an increase in the nucleation density of the h-BN domains. The slower rate of recrystallization resulted in larger Cu crystals with a uniform surface orientation over many millimetres. The rare Cu grain boundaries observed has a minimal effect on the h-BN orientations and the h-BN domains grown at most regions on the resolidified Cu are aligned and the nucleation density is almost homogeneous (Fig. 2d).

Intriguingly, additional shapes with well-defined edges are observed when the h-BN domains nucleate, grow and merge in the same and mirroring orientations. Fig. 3a and b show the SEM images of various complex multifaceted shaped h-BN

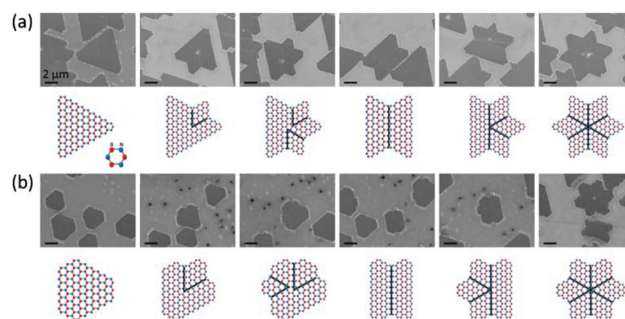


Fig. 3 Complex multifaceted structures of merged h-BN domains. SEM images paired with a schematic illustration of its atomic arrangement (below) displaying various complex structures such as “butterfly” and “six-apex star” of (a) triangular and (b) hexagonal shaped domains. Scale bars are 2 μm. Note the defect lines which are outlined in black in the schematics are prominent in the SEM images.

domains with their corresponding atomic arrangements displayed below. “Rhombus” or “butterfly” shapes are formed by the merging of two mirroring domains and other complex shapes such as “5- and 6-apex star” are evolved from the merging of multiple adjacent domains.^{16,46} Wang *et al.* described that the variety of such complex structures are derived from the two types of merging modes, namely, point-to-edge and edge-to-edge modes.⁴⁶ Both isolated single-crystal domains as well as merged domains are observed all around the Cu surface depending on the distances between nucleation

sites. A single isolated nucleation site forms a single-crystal domain which grows as a triangular or a hexagonal domain. Multifaceted shapes different from those are formed by multiple domains when the nucleation sites are close enough to one another. Many of the secondary shapes contain defect lines²³ which are a consequence of the coalescence between the domains. It is reasonable to suggest that a defect line is formed at the boundary when two mirroring domains with different polarities merge with the same terminating edges. An example is illustrated using a rhombus shaped h-BN structure formed by two mirroring triangles (Fig. S14†). As the polarity

of the domains are different, seamless stitching cannot occur at the grain boundary.

High-resolution (HR) TEM based on a SAED survey gave further insights to the crystalline orientation of the h-BN domains grown on the resolidified Cu. Both single-crystal h-BN domains and fully covered h-BN monolayers are transferred onto TEM grids using a direct transfer approach.⁴⁷ Using this method, the h-BN domains retained their initial orientation as they are directly adhered onto the TEM grid except for some occasional tears. Fig. 4a shows a photograph of a transferred h-BN film on a TEM grid. The boxed regions

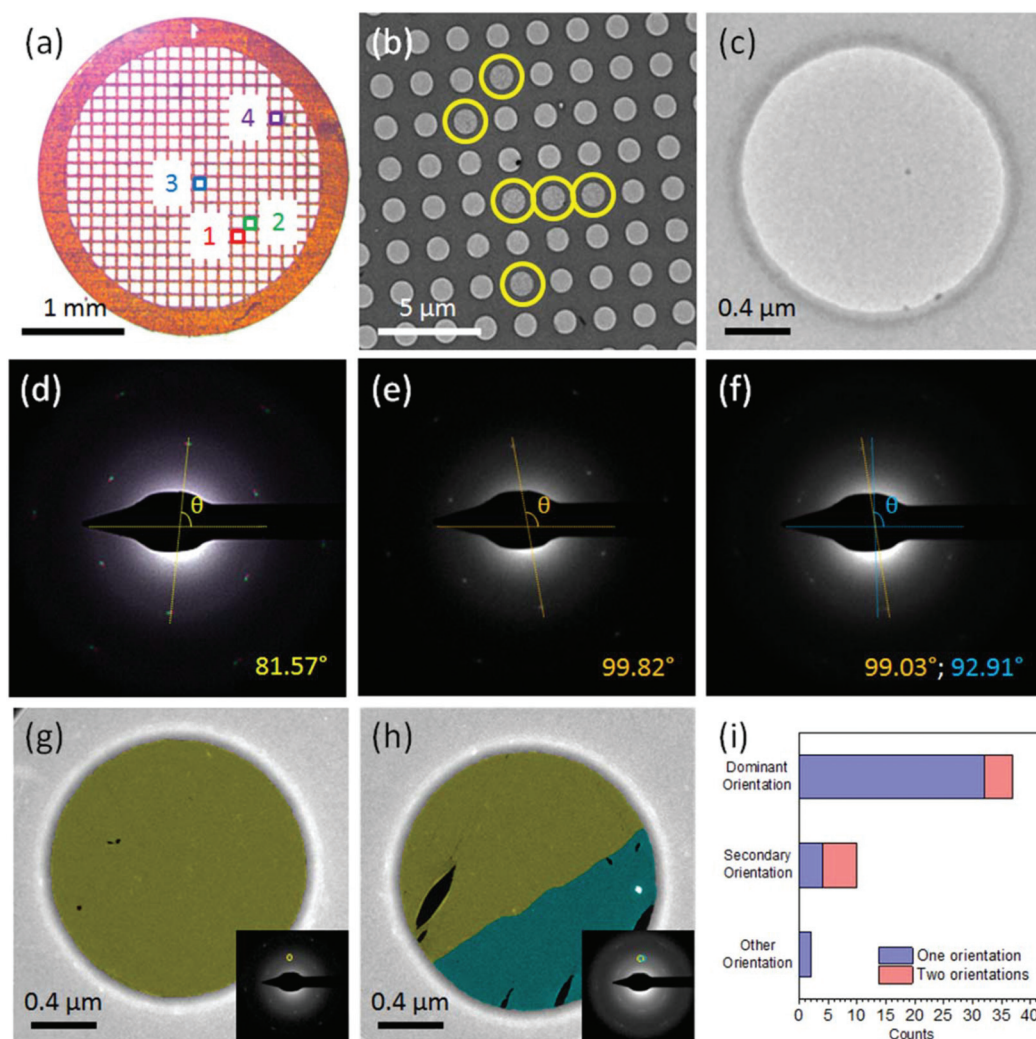


Fig. 4 Millimetre-scale grain mapping of aligned h-BN monolayer. (a) Photograph of a transferred h-BN film on a TEM grid. The squares in regions 1 to 4 indicate the various meshes where multiple SAEDs were conducted. (b) BF-TEM image of the transferred h-BN single-crystal domains on a TEM grid. The yellow circles indicate the presence of h-BN films suspended over several grid holes. (c) Magnified BF-TEM image of a suspended h-BN film over a single grid hole for SAED measurement. (d) Overlay of 7 SAED patterns taken at regions 1 to 4 in (a) exhibiting a dominant orientation. (e) SAED pattern with a "secondary" orientation. (f) SAED pattern with two orientations. The relative angles of the h-BN lattice are indicated at the bottom right were extracted from each SAED pattern by measuring the angle between a straight line connecting two diffraction spots which intersects the centre of the hexagon and a parallel line across the image. False colour DF-TEM images of a (g) mono-crystal and (h) bi-crystal h-BN film comprising of a single orientation and two orientations, respectively. The insets of (g, h) show the corresponding SAED patterns with a coloured circle on a diffracted spot used for DF mapping for each individual grid hole. (i) Statistical plot of the measured relative orientations of 49 SAED patterns.

1 to 4 mark the different meshes where multiple SAEDs were conducted. The furthest distance between two of the marked meshes exceeds 1 mm. Fig. 4b shows a bright-field (BF) TEM image of the isolated h-BN films suspended across various holes that are 1.2 μm in diameter. The free-standing films, which are circled in yellow, showed a slight difference in contrast. The SAED patterns were taken on the h-BN films in each of the individual grid holes as shown in Fig. 4c. $\sim 75\%$ of the SAED patterns showed only one type of diffraction pattern with 6 spots arranged in a particular regular hexagon, indicative of the aligned nature of the film. Fig. 4d shows an overlay of 7 different sets of SAED patterns, taken within regions 1 to 4, composed of the same orientation. This will be referred to as the dominant orientation. It is observed that although most SAED patterns display close alignment, a small fraction showed mis-oriented grains. Fig. 4e and f show two examples of SAED patterns taken on the mis-oriented h-BN grains with one set and two sets of hexagonal diffraction patterns, respectively.

To evaluate the alignment of the h-BN grains, dark-field (DF) TEM, a domain-orientation-sensitive imaging technique, combined with SAED was employed to map the lattice orientation of the h-BN film. Fig. 4g and h show the false colour DF-TEM images of a mono- and bi-crystal h-BN film, respectively. The insets show their respective SAED patterns. The DF-TEM image in Fig. 4g shows no contrast difference and is uniform throughout the suspended h-BN film indicating that there is only one orientation within the grid hole. Defect lines are observed between some aligned h-BN grains that have coalesced (Fig. S15[†]). However, atomic resolution imaging of such defect lines was unsuccessful because the structure is weak and unstable as it is composed of nanoscopic defects and holes were generated very quickly along these defect lines due to knock-on damages by electron radiation. Indeed, it is well-documented that triangular holes are initiated by monovacancies and they grow larger upon prolonged TEM exposure.^{48,49} In the case of mis-aligned h-BN grains with two different orientations, an obvious difference in contrast can be observed as shown in Fig. 4h constituting a h-BN grain with a dominant orientation (in yellow) and a mis-aligned grain (in blue). As such mis-aligned grains coalesce, grain boundary defects due to mis-oriented in-plane stitching will be present.¹⁰

In order to further investigate the occurrences of such mis-orientations, a total of three different sets of SAED measurements were compiled by extracting the relative orientation in each SAED pattern for single-crystal h-BN domains (Table S1[†]) and fully covered h-BN films (Tables S2 and S3[†]). The statistical plot for a total of 49 SAED patterns is shown in Fig. 4i. It is observed that 75.5% of the surveyed area exhibits a dominant orientation with a standard deviation not exceeding 2.25°. Among these, 13.5% of the SAED patterns showed two orientations caused by the merging with the mis-aligned grains. 20.4% of the regions sampled had a different orientation to the dominant but with an identical “secondary” orientation, indicating that the h-BN domains follow a strict epitaxial relationship with the Cu lattice.

There are two possible explanations to account for the “secondary” orientation observed: (i) for epitaxial h-BN growth on Cu(110), there are two preferential superstructures with rotational difference of 30° and (ii) twinning of the Cu lattice after resolidification. For the Cu(110) surface, the two possible h-BN superstructures are: (1 \times 6) and (7 \times 5) structures, as shown in Fig. 1f. Since the (1 \times 6) structure is statistically more favourable,⁴⁴ it is reasonable to conclude that this structure is responsible for the dominant orientation ($\sim 75\%$) observed in our TEM study. $\sim 12\%$ of the total area analyzed had a similar mis-orientation between 25.94° and 32.30° in accord with the 30° mis-match between the (1 \times 6) and (7 \times 5) structures. The occurrence ratio between these two structures is 6.17 : 1, close to the 6 : 1 weight ratio observed on Ni(110).⁴⁴ In addition, through careful SEM inspection, very few h-BN domains which are 30° mis-rotated from the dominant orientation can be identified (Fig. S16[†]). However, there are also some SAED patterns showing orientations different from the dominant and 30° mis-orientation. This could be due to twinning of the Cu lattice.³³ During the resolidification of Cu, twinning of the Cu lattice sometimes occurs which leads to a change in orientation as compared to the parent lattice. Since h-BN is grown epitaxially on the Cu surface, the orientation of h-BN will follow the orientation of the twinned surface. Such clusters of SAED patterns with a similar degree of mis-orientation taken from adjacent TEM grid holes have been observed (Fig. S17[†]).

The polycrystalline nature of the aligned film is unable to be identified by “patchwork quilt” imaging. Note that the mirroring domains with 60° rotational difference will have an identical SAED pattern with little or no change in contrast in their DF-TEM image. A good estimate to extract the grain sizes and the degree of polycrystallinity in such films can be achieved through SEM inspection to identify the presence of grain boundaries or defect lines in merged grains (Fig. S18[†]). Although the average size of an individual domain is $\sim 10 \mu\text{m}$, it is observed that there are many regions with multiple nucleation sites within the range of a single domain. Therefore, the grain sizes (before encountering a grain boundary) in the films are not more than 10 μm .

The aligned h-BN films of over centimetre-size were used for further characterisation. The as-grown h-BN films were transferred onto SiO₂/Si and quartz substrates using poly (methyl-methacrylate) (PMMA) either by a wet transfer approach⁵⁰ or through electrochemical delamination.⁵¹ Fig. 5a shows the optical images of the transferred film on SiO₂/Si at the edge with folded regions (due to transfer process) and at the centre. The AFM image in Fig. 5b shows that the h-BN film is very smooth with a root-mean-square (RMS) roughness of $\sim 0.42 \text{ nm}$ and an estimated step height of $\sim 0.58 \text{ nm}$ corresponding to a monolayer. Fig. 5c shows an atomic resolution TEM image of the h-BN film displaying its hexagonal structure. Nano-sized triangular holes are commonly observed on the film due to knock-on damage caused by electron irradiation during TEM imaging,⁴⁹ which further confirm the monolayer nature of the film. Fig. 5d shows the Raman spectrum of a transferred h-BN film on the SiO₂/Si substrate with a sharp

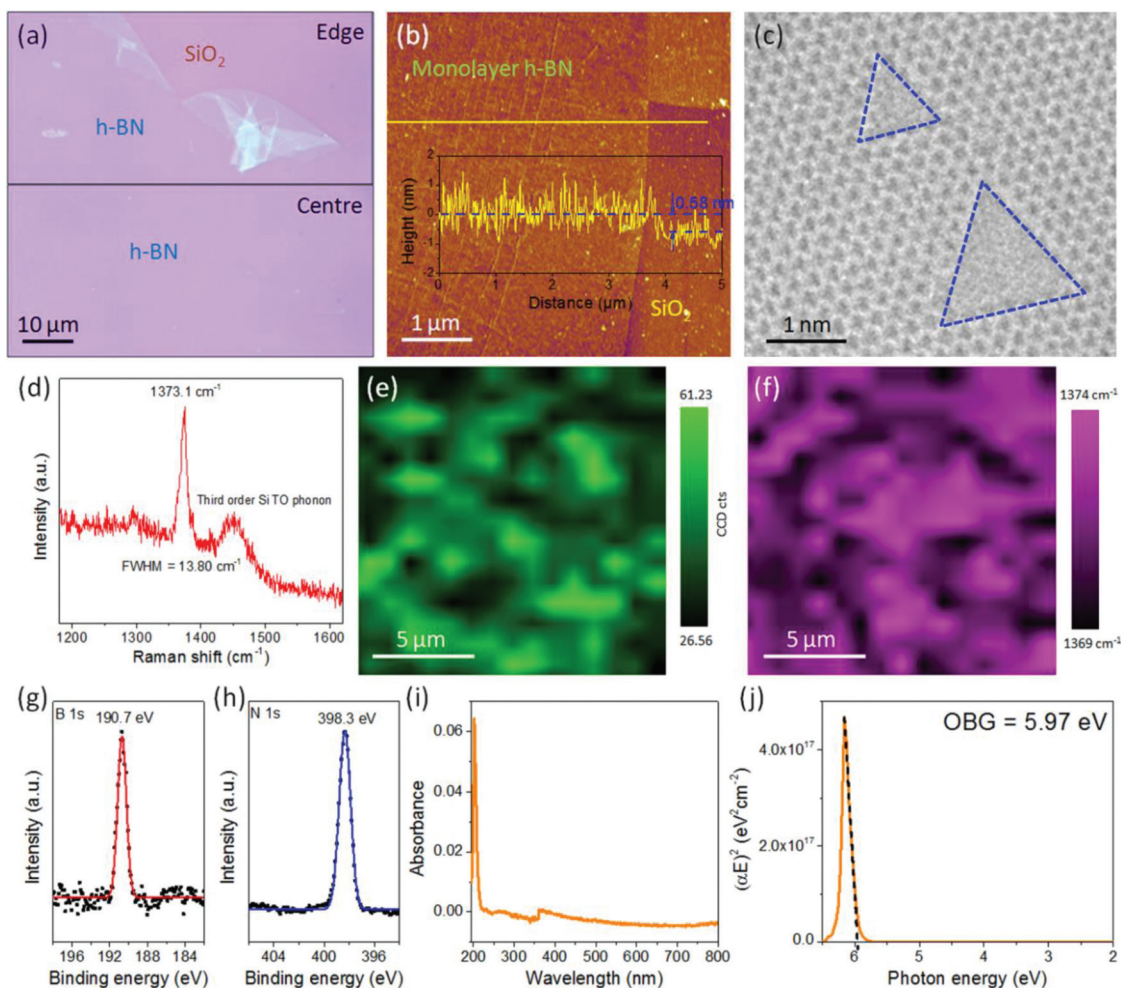


Fig. 5 Characterisation of aligned h-BN film grown on resolidified Cu. (a) Optical image taken at the edge and centre of a transferred monolayer h-BN film on the SiO₂/Si substrate. (b) AFM image at a boundary between the h-BN film and SiO₂ surface with a measured RMS roughness of ~ 0.42 nm and thickness of 0.58 nm (inset). (c) Top-view HR-TEM image of a monolayer h-BN film exhibiting hexagonal atomic arrangement with triangular holes outlined in blue. (d) Representative Raman spectrum with peak position at 1373.1 cm^{-1} and a fitted FWHM of 13.80 cm^{-1} . Representative Raman mapping of the (e) peak intensity and (f) peak position ranging from 1369 to 1374 cm^{-1} within a $15\text{ }\mu\text{m} \times 15\text{ }\mu\text{m}$ scanned area. XPS spectra for (g) B 1s and (h) N 1s. (i) Absorbance spectrum measured using UV-vis spectroscopy with a sharp peak at 202 nm. (j) Plot of $(\alpha E)^2$ against E for OBG extraction. The extrapolated dotted black line indicates an OBG of 5.97 eV.

peak at 1373.1 cm^{-1} , corresponding to the E_{2g} vibration mode of a h-BN monolayer,^{7,52} and a full width at half maximum (FWHM) of 13.80 cm^{-1} (Fig. S19†). Fig. 5e and f show the representative Raman maps of the maximum peak intensity and peak position over an area of $15\text{ }\mu\text{m} \times 15\text{ }\mu\text{m}$, respectively. For fully covered h-BN films, because of its non-self-limited growth mechanism, the amount of bi- to few-layer islands is ~ 2 to 13.5% as determined by SEM due to the varying CVD parameters (Fig. S2d and S3d†). These multilayer islands are detected by Raman mapping which reveals non-uniformity in both line intensity and peak position. The Raman peak intensity increases and its position slightly downshifts when the number of h-BN layers increases.⁵² It should also be noted that as the Raman signal for h-BN is weak, noise is also a contributing factor for the observed dis-uniformity. For the h-BN single crystals, both AFM and Raman scans confirm that the domains

are uniform and composed of a single layer (Fig. S20†). XPS measurements show a single peak for both B 1s and N 1s at 190.7 and 398.3 eV, as shown in Fig. 5g and h, respectively, confirming the presence of the B–N bond.⁵³ The B:N elemental stoichiometry extracted based on the integral intensities of the characteristic peaks is $\sim 1:1.05$. Ultraviolet-visible (UV-vis) absorption spectroscopy was used to determine the optical band gap (OBG) of the h-BN film on the quartz substrate. Fig. 5i shows the UV-vis absorption spectrum with an abrupt absorption peak at 202 nm. To extract the OBG of the film, the absorbance spectrum is converted into Tauc's plot as shown in Fig. 5j using the derived formula for a direct band gap semiconductor (Fig. S21†).⁵⁴ An OBG of $\sim 5.97\text{ eV}$ is obtained which is very close to the theoretical value of 6.0 eV for monolayer h-BN.⁵⁵

Although the aligned growth of h-BN domains has been achieved in this study, the challenge of seamless stitching in

this “multi-nucleation” approach still remains. Defect lines are commonly observed at the boundaries between mirroring domains. Unlike graphene where it consists solely of C atoms, h-BN has a binary configuration composed of B and N atoms. This gives rise to two different polarities. It has been deduced through a simple geometric structure of h-BN domains that seamless stitching cannot occur between the domains with different polarities. Furthermore, it has been reported that the terminating edges of the h-BN domains are predominantly in the zigzag configuration and the domains are usually triangular.^{4,13} N-terminated edges are calculated to be energetically more favourable than B-terminated edges,⁵⁶ and based on this calculation, the triangular domains are explained to have all N-terminated zigzag sides. Seamless stitching between the h-BN domains could be further impeded when they converge with the same edge termination. Recently, Yin *et al.*⁵⁷ and Wu *et al.*²¹ reported seamless stitching between aligned h-BN domains when the polarities of the domains are the same (not in mirroring orientations). Hence, it is possible to obtain a large single crystalline h-BN film with minimal grain boundaries if one could control the polarity of the h-BN during nucleation.

The present work shows that the h-BN domains are often asymmetric hexagons (truncated triangles). In theory, the sides of a hexagonal domain can consist of either alternating N- and B-terminated zigzag edges or armchair edges. For an asymmetric hexagonal domain, the growth mechanism can be explained by the Wulff construction in which a crystal obtains an equilibrium shape with a minimum edge (or surface) energy.⁵⁸ There exists a point in the interior where the perpendicular distance, h_i , from the i th edge is proportional to the edge energy, E_i , as given by $E_i = Ch_i$, where C is a constant and i represents either N- or B-terminated zigzag edges. $E_B > E_N$, so that, $h_B > h_N$ (Fig. S22†). As such, the observed asymmetric hexagons are actually triangles with their apexes being “cut” to minimize the energy. Upon closer inspection at the SEM images of the triangular shaped domain, the tips of the triangles can also be seen to be truncated in accordance with the Wulff construction (Fig. S23†), with the short edges as B-terminated and the long edges as N-terminated. In the case of symmetric hexagons where all sides are of equal length, their edge energies are required to be similar. This potentially implies an armchair edge configuration for hexagonal shaped domains.^{56,59} It is noteworthy that E_i may change due to variations such as the existence of H-terminations,^{59,60} and the presence of surface oxygen of the Cu substrates,⁶¹ which could account for the different extents of the non-equilateral hexagonal shaped domains observed.

Conclusions

In summary, monolayer h-BN single-crystal domains of up to ~10 μm which are aligned for over centimetre-scale are grown on resolidified Cu using APCVD. Full coverage h-BN films with a dominant orientation over their entire range can be further

obtained by increasing the growth time. SAED and DF-TEM imaging reveals that ~75% of the h-BN grains have the same orientation due to a well defined epitaxial relationship between the h-BN lattice and that of Cu(110). The strong alignment of the individual domain islands leads to their convergence to symmetrical multifaceted structures including “butterfly” and “6-apex star”. The shapes of the single-crystal domains are in the form of triangles with truncated edges and hexagons, in accordance with Wulff shapes with minimum edge energy. Defect lines are formed at the boundaries between mirroring domains due to the polarity difference and domains with the same terminating edges. This work reveals the challenges of in-plane stitching for materials with a binary configuration and highlights the obstacles that are needed to be overcome in order to attain a truly high quality single crystalline film over large distances.

Acknowledgements

We acknowledge the funding support from NTU-A*STAR Silicon Technologies Centre of Excellence under the program grant no. 1123510003, Singapore Ministry of Education Academic Research Fund Tier 2 no. MOE2013-T2-2-050 and the Nano Material Technology Development Program through the National Research Foundation of Korea (NRF) funded by the Ministry of Science, ICT and Future Planning (2012M3A7B4049807). R. S. R. and Z. L. acknowledge the support by IBS-R019-D1.

Notes and references

- 1 C. R. Dean, A. F. Young, I. Meric, C. Lee, L. Wang, S. Sorgenfrei, K. Watanabe, T. Taniguchi, P. Kim, K. L. Shepard and J. Hone, *Nat. Nanotechnol.*, 2010, **5**, 722–726.
- 2 L. Britnell, R. V. Gorbachev, R. Jalil, B. D. Belle, F. Schedin, A. Mishchenko, T. Georgiou, M. I. Katsnelson, L. Eaves, S. V. Morozov, N. M. R. Peres, J. Leist, A. K. Geim, K. S. Novoselov and L. A. Ponomarenko, *Science*, 2012, **335**, 947–950.
- 3 G. Shi, Y. Hanlumyuang, Z. Liu, Y. Gong, W. Gao, B. Li, J. Kono, J. Lou, R. Vajtai, P. Sharma and P. M. Ajayan, *Nano Lett.*, 2014, **14**, 1739–1744.
- 4 K. K. Kim, A. Hsu, X. Jia, S. M. Kim, Y. Shi, M. Hofmann, D. Nezich, J. F. Rodriguez-Nieva, M. Dresselhaus, T. Palacios and J. Kong, *Nano Lett.*, 2012, **12**, 161–166.
- 5 L. Song, L. Ci, H. Lu, P. B. Sorokin, C. Jin, J. Ni, A. G. Kvashnin, D. G. Kvashnin, J. Lou, B. I. Yakobson and P. M. Ajayan, *Nano Lett.*, 2010, **10**, 3209–3215.
- 6 Y. Shi, C. Hamsen, X. Jia, K. K. Kim, A. Reina, M. Hofmann, A. L. Hsu, K. Zhang, H. Li, Z.-Y. Juang, M. S. Dresselhaus, L.-J. Li and J. Kong, *Nano Lett.*, 2010, **10**, 4134–4139.

- 7 G. Kim, A. R. Jang, H. Y. Jeong, Z. Lee, D. J. Kang and H. S. Shin, *Nano Lett.*, 2013, **13**, 1834–1839.
- 8 S. M. Kim, A. Hsu, M. H. Park, S. H. Chae, S. J. Yun, J. S. Lee, D.-H. Cho, W. Fang, C. Lee, T. Palacios, M. Dresselhaus, K. K. Kim, Y. H. Lee and J. Kong, *Nat. Commun.*, 2015, **6**, 8662.
- 9 Z. Liu, Y. Gong, W. Zhou, L. Ma, J. Yu, J. C. Idrobo, J. Jung, A. H. MacDonald, R. Vajtai, J. Lou and P. M. Ajayan, *Nat. Commun.*, 2013, **4**, 2541.
- 10 A. L. Gibb, N. Alem, J.-H. Chen, K. J. Erickson, J. Ciston, A. Gautam, M. Linck and A. Zettl, *J. Am. Chem. Soc.*, 2013, **135**, 6758–6761.
- 11 V. L. Nguyen, B. G. Shin, D. L. Duong, S. T. Kim, D. Perello, Y. J. Lim, Q. H. Yuan, F. Ding, H. Y. Jeong, H. S. Shin, S. M. Lee, S. H. Chae, Q. A. Vu, S. H. Lee and Y. H. Lee, *Adv. Mater.*, 2015, **27**, 1376–1382.
- 12 V. L. Nguyen and Y. H. Lee, *Small*, 2015, **11**, 3512–3528.
- 13 L. Wang, B. Wu, J. Chen, H. Liu, P. Hu and Y. Liu, *Adv. Mater.*, 2014, **26**, 1559–1564.
- 14 G. Lu, T. Wu, Q. Yuan, H. Wang, H. Wang, F. Ding, X. Xie and M. Jiang, *Nat. Commun.*, 2015, **6**, 6160.
- 15 S. Caneva, R. S. Weatherup, B. C. Bayer, B. Brennan, S. J. Spencer, K. Mingard, A. Cabrero-Vilatela, C. Baecht, A. J. Pollard and S. Hofmann, *Nano Lett.*, 2015, **15**, 1867–1875.
- 16 J. Yin, J. Yu, X. Li, J. Li, J. Zhou, Z. Zhang and W. Guo, *Small*, 2015, **11**, 4497–4502.
- 17 X. Song, J. Gao, Y. Nie, T. Gao, J. Sun, D. Ma, Q. Li, Y. Chen, C. Jin, A. Bachmatiuk, M. H. Rummeli, F. Ding, Y. Zhang and Z. Liu, *Nano Res.*, 2015, **8**, 3164–3176.
- 18 R. Y. Tay, X. Wang, S. H. Tsang, G. C. Loh, R. S. Singh, H. Li, G. Mallick and E. H. T. Teo, *J. Mater. Chem. C*, 2014, **2**, 1650–1657.
- 19 N. Guo, J. Wei, L. Fan, Y. Jia, D. Liang, H. Zhu, K. Wang and D. Wu, *Nanotechnology*, 2012, **23**, 41.
- 20 P. R. Kidambi, R. Blume, J. Kling, J. B. Wagner, C. Baecht, R. S. Weatherup, R. Schloegl, B. C. Bayer and S. Hofmann, *Chem. Mater.*, 2014, **26**, 6380–6392.
- 21 Q. Wu, J.-H. Park, S. Park, S. J. Jung, H. Suh, N. Park, W. Wongwiriyan, S. Lee, Y. H. Lee and Y. J. Song, *Sci. Rep.*, 2015, **5**, 16159.
- 22 R. Y. Tay, M. H. Griep, G. Mallick, S. H. Tsang, R. S. Singh, T. Tumlin, E. H. T. Teo and S. P. Karna, *Nano Lett.*, 2014, **14**, 839–846.
- 23 W. Auwärter, M. Muntwiler, J. Osterwalder and T. Greber, *Surf. Sci.*, 2003, **545**, 735–740.
- 24 W. Auwärter, H. U. Suter, H. Sachdev and T. Greber, *Chem. Mater.*, 2004, **16**, 343–345.
- 25 C. Zhang, L. Fu, S. Zhao, Y. Zhou, H. Peng and Z. Liu, *Adv. Mater.*, 2014, **26**, 1776–1781.
- 26 Y. Gao, W. Ren, T. Ma, Z. Liu, Y. Zhang, W.-B. Liu, L.-P. Ma, X. Ma and H.-M. Cheng, *ACS Nano*, 2013, **7**, 5199–5206.
- 27 L. Camilli, E. Sutter and P. Sutter, *2D Mater.*, 2014, **1**, 025003.
- 28 L. Brown, E. B. Lochocki, J. Avila, C.-J. Kim, Y. Ogawa, R. W. Havener, D.-K. Kim, E. J. Monkman, D. E. Shai, H. I. Wei, M. P. Levendorf, M. Asensio, K. M. Shen and J. Park, *Nano Lett.*, 2014, **14**, 5706–5711.
- 29 L. Liu, D. A. Siegel, W. Chen, P. Liu, J. Guo, G. Duscher, C. Zhao, H. Wang, W. Wang, X. Bai, K. F. McCarty, Z. Zhang and G. Gu, *Proc. Natl. Acad. Sci. U. S. A.*, 2014, **111**, 16670–16675.
- 30 G. E. Wood, A. J. Marsden, J. J. Mudd, M. Walker, M. Asensio, J. Avila, K. Chen, G. R. Bell and N. R. Wilson, *2D Mater.*, 2015, **2**, 025003.
- 31 S. Joshi, D. Eciija, R. Koitz, M. Iannuzzi, A. P. Seitsonen, J. Hutter, H. Sachdev, S. Vijayaraghavan, F. Bischoff, K. Seufert, J. V. Barth and W. Auwärter, *Nano Lett.*, 2012, **12**, 5821–5828.
- 32 D. Geng, B. Wu, Y. Guo, L. Huang, Y. Xue, J. Chen, G. Yu, L. Jiang, W. Hu and Y. Liu, *Proc. Natl. Acad. Sci. U. S. A.*, 2012, **109**, 7992–7996.
- 33 Y. A. Wu, Y. Fan, S. Speller, G. L. Creeth, J. T. Sadowski, K. He, A. W. Robertson, C. S. Allen and J. H. Warner, *ACS Nano*, 2012, **6**, 5010–5017.
- 34 A. Mohsin, L. Liu, P. Liu, W. Deng, I. N. Ivanov, G. Li, O. E. Dyck, G. Duscher, J. R. Dunlap, K. Xiao and G. Gu, *ACS Nano*, 2013, **7**, 8924–8931.
- 35 B. Wu, D. Geng, Z. Xu, Y. Guo, L. Huang, Y. Xue, J. Chen, G. Yu and Y. Liu, *NPG Asia Mater.*, 2013, **5**, e36.
- 36 D. Geng, L. Meng, B. Chen, E. Gao, W. Yan, H. Yan, B. Luo, J. Xu, H. Wang, Z. Mao, Z. Xu, L. He, Z. Zhang, L. Peng and G. Yu, *Adv. Mater.*, 2014, **26**, 6423–6429.
- 37 M. H. Khan, Z. Huang, F. Xiao, G. Casillas, Z. Chen, P. J. Molino and H. K. Liu, *Sci. Rep.*, 2015, **5**, 7743.
- 38 D. Geng, B. Luo, J. Xu, Y. Guo, B. Wu, W. Hu, Y. Liu and G. Yu, *Adv. Funct. Mater.*, 2014, **24**, 1664–1670.
- 39 L. Tan, J. Han, R. G. Mendes, M. H. Rummeli, J. Liu, Q. Wu, X. Leng, T. Zhang, M. Zeng and L. Fu, *Adv. Electron. Mater.*, 2015, **1**(11), DOI: 10.1002/aelm.201500223.
- 40 Y. Stehle, H. M. Meyer, R. R. Unocic, M. Kidder, G. Polizos, P. G. Datskos, R. Jackson, S. N. Smirnov and I. V. Vlassioug, *Chem. Mater.*, 2015, **27**, 8041–8047.
- 41 H. Wormeester, M. E. Kiene, E. Hüger and E. Bauer, *Surf. Sci.*, 1997, **377–379**, 988–991.
- 42 E. Bauer, H. Poppa, G. Todd and F. Bonczek, *J. Appl. Phys.*, 1974, **45**, 5164–5175.
- 43 G. A. Attard and D. A. King, *Surf. Sci.*, 1987, **188**, 589–598.
- 44 T. Greber, L. Brandenberger, M. Corso, A. Tamai and J. Osterwalder, *e-J. Surf. Sci. Nanotechnol.*, 2006, **4**, 410–413.
- 45 J. Beddoes and M. J. Bibby, in *Principles of Metal Manufacturing Processes*, ed. J. Beddoes and M. J. Bibby, Butterworth-Heinemann, Oxford, 1999, pp. 18–66.
- 46 L. Wang, B. Wu, L. Jiang, J. Chen, Y. Li, W. Guo, P. Hu and Y. Liu, *Adv. Mater.*, 2015, **27**, 4858.
- 47 W. Regan, N. Alem, B. Alemán, B. Geng, Ç. Girit, L. Maserati, F. Wang, M. Crommie and A. Zettl, *Appl. Phys. Lett.*, 2010, **96**, 113102.
- 48 J. Kotakoski, C. H. Jin, O. Lehtinen, K. Suenaga and A. V. Krasheninnikov, *Phys. Rev. B: Condens. Matter*, 2010, **82**, 113404.

- 49 G. H. Ryu, H. J. Park, J. Ryou, J. Park, J. Lee, G. Kim, H. S. Shin, C. W. Bielawski, R. S. Ruoff, S. Hong and Z. Lee, *Nanoscale*, 2015, **7**, 10600–10605.
- 50 X. Li, Y. Zhu, W. Cai, M. Borysiak, B. Han, D. Chen, R. D. Piner, L. Colomboa and R. S. Ruoff, *Nano Lett.*, 2009, **9**, 4359–4363.
- 51 L. Gao, W. Ren, H. Xu, L. Jin, Z. Wang, T. Ma, L.-P. Ma, Z. Zhang, Q. Fu, L.-M. Peng, X. Bao and H.-M. Cheng, *Nat. Commun.*, 2012, **3**, 699.
- 52 R. V. Gorbachev, I. Riaz, R. R. Nair, R. Jalil, L. Britnell, B. D. Belle, E. W. Hill, K. S. Novoselov, K. Watanabe, T. Taniguchi, A. K. Geim and P. Blake, *Small*, 2011, **7**, 465–468.
- 53 R. Trehan, Y. Lifshitz and J. W. Rabalais, *J. Vac. Sci. Technol., A*, 1990, **8**, 4026–4032.
- 54 T. H. Yuzuriha and D. W. Hess, *Thin Solid Films*, 1986, **140**, 199–207.
- 55 X. Blase, A. Rubio, S. G. Louie and M. L. Cohen, *Phys. Rev. B: Condens. Matter*, 1995, **51**, 6868–6875.
- 56 Y. Liu, S. Bhowmick and B. I. Yakobson, *Nano Lett.*, 2011, **11**, 3113–3116.
- 57 J. Yin, X. Liu, W. Lu, J. Li, Y. Cao, Y. Li, Y. Xu, X. Li, J. Zhou, C. Jin and W. Guo, *Small*, 2015, **11**, 5375–5380.
- 58 G. Wulff and Z. Krist, *Krystallogr. Mineral.*, 1901, **34**, 449.
- 59 R. Zhao, J. Gao, Z. Liu and F. Ding, *Nanoscale*, 2015, **7**, 9723–9730.
- 60 C. Gan and D. Srolovitz, *Phys. Rev. B: Condens. Matter*, 2010, **81**, 125445.
- 61 Y. Hao, M. S. Bharathi, L. Wang, Y. Liu, H. Chen, S. Nie, X. Wang, H. Chou, C. Tan, B. Fallahazad, H. Ramanarayan, C. W. Magnuson, E. Tutuc, B. I. Yakobson, K. F. McCarty, Y.-W. Zhang, P. Kim, J. Hone, L. Colombo and R. S. Ruoff, *Science*, 2013, **342**, 720–723.